# Negative Differential Resistance in Carbon-Based Nanostructures

S.A. Evlashin[1] M.A. Tarkhov,[2] D.A. Chernodubov,[3] A.V. Inyushkin,[3] A.A. Pilevsky,[4]
P.V. Dyakonov,[1,4] A.A. Pavlov,[2] N.V. Suetin,[4] I.S. Akhatov,[1] and V. Perebeinos[5,*]

[1]*Center for Design, Manufacturing and Materials, Skolkovo Institute of Science and Technology,
Moscow 121205, Russia*
[2]*Institute of Nanotechnology of Microelectronics of the Russian Academy of Sciences, Moscow 119991, Russia*
[3]*National Research Center "Kurchatov Institute," Moscow 123182, Russia*
[4]*Skobel'tsyn Institute of Nuclear Physics, Lomonosov Moscow State University, Moscow 119991, Russia*
[5]*Department of Electrical Engineering, University at Buffalo, The State University of New York, Buffalo,
New York 14260, USA*

Nonlinear electrical properties, such as negative differential resistance (NDR), are essential in numerous electrical circuits, including memristors. Several physical origins have been proposed to lead to the NDR phenomena in semiconductor devices over the last more than half a century. Here, we report NDR behavior formation in randomly oriented graphenelike nanostructures up to 37 K and high on-current density up to $10^5$ A/cm$^2$. Our modeling of the current-voltage characteristics, including the self-heating effects, suggests that strong temperature dependence of the low-bias resistance is responsible for the nonlinear electrical behavior. Our findings open opportunities for the practical realization of the on-demand NDR behavior in nanostructures of two- and three-dimensional material-based devices via heat management in the conducting films and the underlying substrates.

## I. INTRODUCTION

Nonlinear electrical characteristics allow the design of devices with unique properties. In particular, the realization of such components and devices as electronic circuitry, storage memory, electric switches, wave generators, power generators, and multipliers [1–4]. Most commonly, two-terminal Schottky diodes, Esaki diodes, and Gunn diodes [5,6] exhibit nonlinear electrical characteristics. Three-terminal field-effect transistors with nonlinear characteristics have also been demonstrated [7–9]. The interest in nonlinear electrical devices was revived after an experimental demonstration of a memristor by the HP lab [10]. Recently, devices with highly nonlinear current-voltage characteristics found applications as selectors in crossbar memory arrays [11,12]. However, the significant obstacles in applications include the poor on-current density, integration challenges, and manufacturing cost.

Unlike "Ohmic" resistances, negative differential resistance (NDR) demonstrates an increase of current at a decrease of voltage and vice versa. NDR is of particular interest, among the other nonlinear properties. Depending on the *I-V* curve shape, NDR can be of N-type voltage control or S-type current control [13]. Recently, NDR devices have been realized on different oxide films [14–20],

semiconductor heterostructures [21,22], single molecules [1,23,24], two-dimensional materials, and their combinations [3,25–30]. The origins of the NDR behavior can be due to the band structure effects, phonon blockade, chemical reactions, heat management, electrical contacts, to name a few [1–30].

NDR behavior in metal oxide films has attracted much interest [31–33]. The S-type NDR in such systems is associated with the formation of current density domains parallel to the electric field [34] and Poole-Frenkel effects [31]. Poole-Frenkel model describes the NDR in the NbO$_x$ films [31] by the presence of donors and traps. In TiO films, the NDR was explained by the Joule heating and polaronic transport [32]. In the recent theoretical work [35], the authors demonstrated the influence of the Joule heating on NDR and compared their results with the earlier findings [2,36]. They concluded that strong temperature dependence of the low-bias resistance leads to the onset of NDR. Therefore, in principle, NDR can result from any transport mechanism as long as thermal runaway occurs in sustainable fields and temperatures.

Carbon nanostructures can also demonstrate nonlinear characteristics. NDR was reported in mono- and multi-layered graphene films, defective and *n*-doped graphene, and graphene-oxide carbon nanotubes [3,9,29,30,37–42]. The NDR in the defected or doped graphene layer is attributed to a change in the band structure [29,30]. In
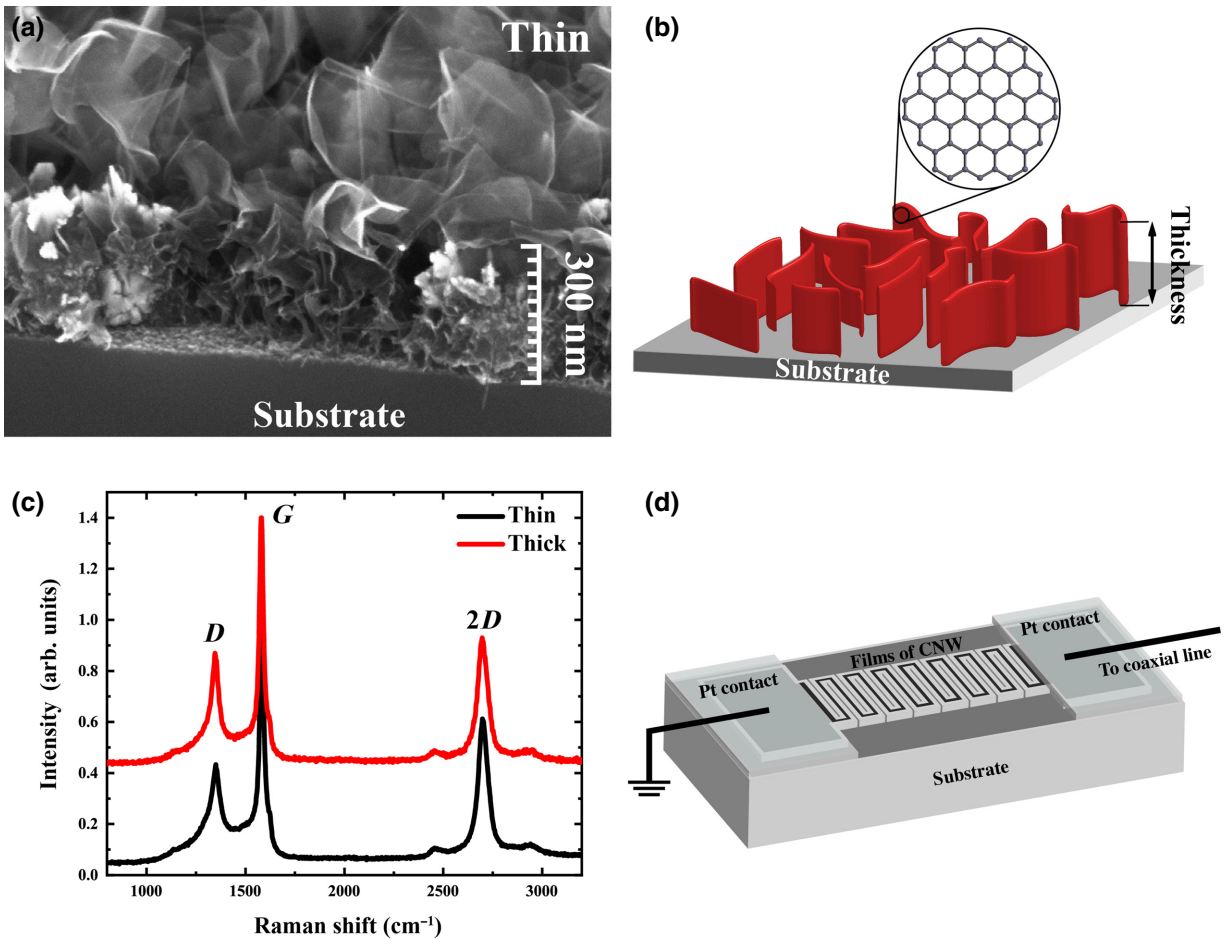
---

*vasilipe@buffalo.edu

FIG. 1. (a) SEM image of CNWs synthesized for 20 min. (b) schematic of CNWs film morphology (c) Raman spectra of samples of various synthesis times, and (d) a schematic representation of the measuring device.

graphene nanoribbons, it was attributed to the interference at zigzag edges [43]. It is well known that carbon has a narrow electrochemical window and can be easily oxidized [44]. In [39], the authors demonstrated NDR in graphene oxide by applying different current densities in the graphene oxide film leading to oxidation and reduction of these films.

This work demonstrates a nanostructure class of materials that possess S-type NDR characteristics and high current density capacity. These materials consist of spongelike carbon-based material called carbon nanowalls (CNWs). Our simulations demonstrate that the direct influence of the Joule losses causes NDR phenomena, and we suggest that thermal management between the film and the substrate interface is essential for the NDR characteristics.

## II. EXPERIMENTAL METHODS

### A. Synthesis of CNWs

CNWs are synthesized on a silicon substrate by direct current plasma-enhanced chemical vapor deposition (DC PECVD) method [45,46]. A mixture of $CH_4$ and $H_2$ flows

at 15 and 200 sccm, respectively, is used as a source gas. The pressure is 150 Torr, and the discharge current is 5.2 A, and synthesis time is 20 min for the thin sample and 60 min for the thick sample.

### B. Structure characterization

The obtained structures are characterized by a Carl Zeiss Supra 40 scanning electron microscopy (SEM) and Raman spectroscopy (Thermo Scientific DXR Raman Microscope spectrometer). For more details, see [47,48].

### C. Fabrication of meander

The laser ablation technique is applied for meander fabrication [49]. Pulse laser TEMA with 1064 nm wavelength, 70 fs pulse duration, laser power 0.1 W with pulse reputation ratio 80 MHz. The meander area is $2 \times 2$ mm$^2$, the line width of 100 $\mu$m with a gap between contacts of 100 $\mu$m.

### D. Current-voltage measurements

The resistivity measurements $R(T)$ are conducted in a Sumitomo Heavy Industries SRDK 101D cryocooler.
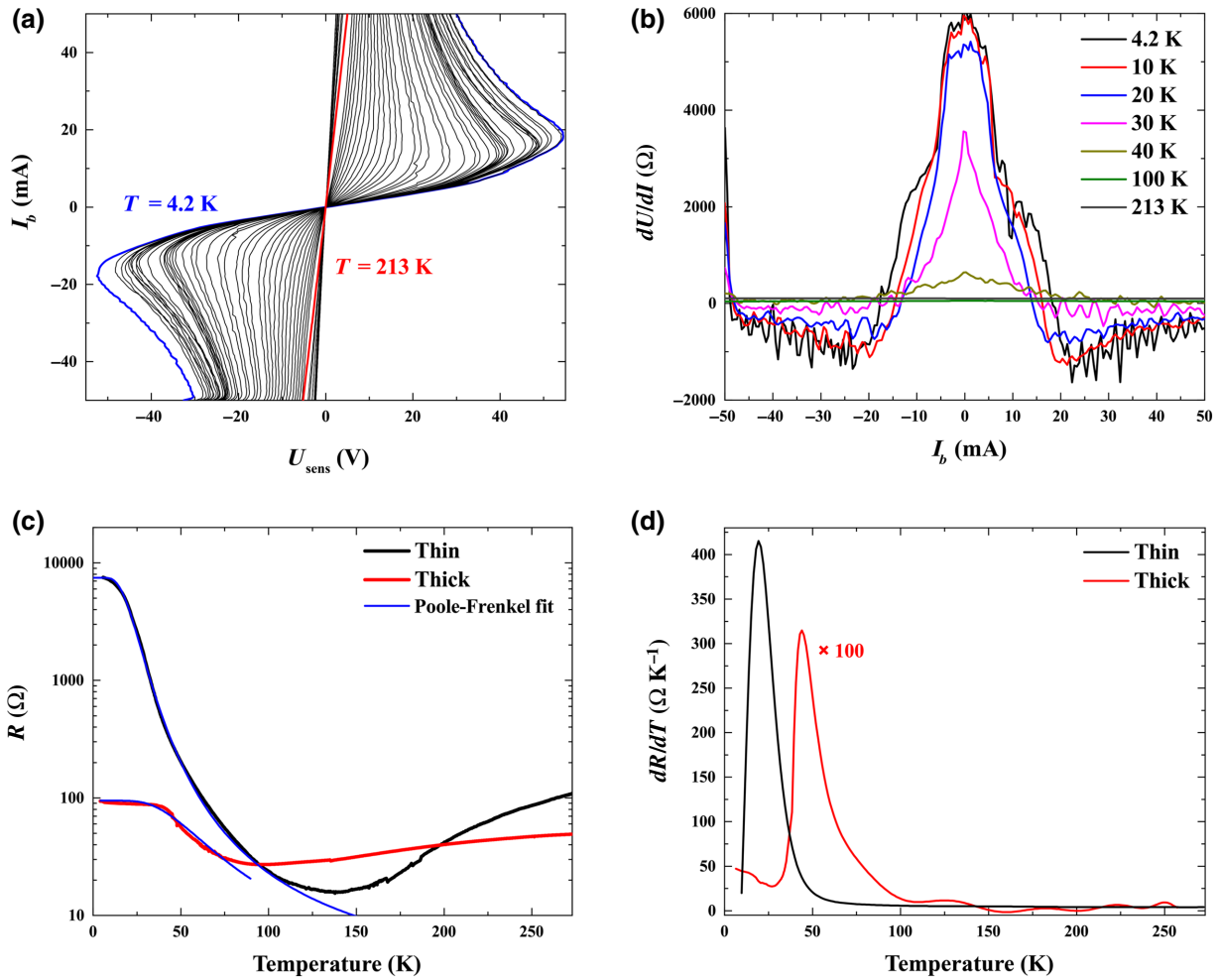
FIG. 2.   (a) The current-voltage characteristics at different ambient temperatures for thin CNWs film, (b) differential resistance at different temperatures thin films of CNWs, (c) temperature dependencies of the low-bias resistance along with the fits to the Poole-Frankel model Eq. (1), and (d) the corresponding temperature dependencies of the low-bias differential resistance $dR/dT$. Note a factor of 100 used for the red curve.

The current-voltage characteristics are measured using a low-noise precision current source Keithley Instruments 2400. Temperature monitoring is conducted by a Lake Shore Cryotronics DT-670-SD temperature controller. This system allows temperature control with a rate of heating/cooling of 1 K/min. The stability range is from 2.3 to 230 K. The current-voltage characteristics are measured at a fixed temperature in the current or voltage stabilization regime. The pressure at the chamber is $10^{-7}$ Torr.

### E. Thermal conductivity measurements

The thermal conductivity is measured using a steady-state longitudinal heat flow method in the temperature range from 5 to 100 K. One end of the sample is fixed in a copper block that serves as a heat sink, whereas a heater is mounted to another end. The temperature gradient is defined as a ratio of the temperature difference between the two points of the sample located along its long axis. The distance between these points is about 3.5 mm. The heat output in the heater is selected so that the relative temperature difference is approximately 0.01. To minimize the heat losses from the heater, the measurements are performed in a vacuum cell with a residual gas pressure of less than $7 \times 10^{-6}$ Torr. The technique used is similar to that described in Ref. [50] with an exception: in this work, the temperature gradient is measured using a pair of Cernox CX-1050 resistance temperature sensors (Lake Shore Cryotronics, Inc.), whereas in Ref. [50] the thermocouples were utilized. The thermal conductivity of the film is found from the difference in the thermal conductivities of the substrate measured with and without the film. During the measurements, the film from the quartz substrate is removed mechanically *in situ*, without demounting the sample from the measuring cell.

## III. RESULTS

An SEM image of the thin film of CNWs is shown in Fig. 1(a), and a schematic representation of the film morphology is shown in Fig. 1(b). The thick film has the same structure, except for the thickness is about 1 $\mu$m. The corresponding Raman spectra for thin and thick films are shown in Fig. 1(c). A defect ratio of the carbon structures depends on the synthesis parameters. The intensity ratio of the $D$ to $G$ peaks changes from 1.27 to 1.10, which corresponds to a change in an average crystallite size from 15.0 to 17.4 nm [51,52]. Similar dependencies are observed for the intensity ratio of $2D$ to $G$ peaks, which changes from 1.22 to 1.11.

A schematic image of the electrical device is shown in Fig. 1(d). The current-voltage characteristic ($I$-$V$ curve) for the thin film demonstrates a NDR at temperatures lower than 37 K, as shown in Fig. 2(a). Note that the current density in our device operating in NDR regime reaches values of up to $10^5$ A/cm$^2$. At the same time, the thick film of 1000 nm thickness does not show such behavior. The measured $I$-$V$ curves on the thick films show Ohmic dependencies and are not shown in the manuscript.

Figure 2(b) demonstrates the temperature and bias regime when NDR is most pronounced. Figure 2(c) shows the temperature dependencies of the low-bias electrical resistance. A similar shape of dependencies is observed for CNWs by other researchers [53]. For the thin film, the resistance reaches its minimum value at 130 K, and the differential resistance $dR/dT$ shows a peak at around 21 K, as shown in Fig. 2(d) by the black curve. The thick film demonstrates the minimal resistance at 90 K, and the maximum differential resistance at a much smaller value than the thin film, as shown in Fig. 2(d) by the red curve.

TABLE I. Fitting parameters for the Poole-Frankel model in Eq. (1).

| | Thickness (nm) | $R(0)$ ($\Omega$) | $T_t$ (K) | $c$ | $n$ |
|---|---|---|---|---|---|
| Thin | 400 | 7470 | 360 | 1790 | 0.2 |
| Thick | 1000 | 94.7 | 360 | 61.8 | 0.474 |

Previous studies have shown that a considerable temperature gradient is responsible for the formation of S-type NDR in oxide films [18]. The formation of high-current density domains and thermally activated Poole-Frankel conductivity, together with the Joule heating, lead to the NDR behavior in oxide films [18]. This Joule heating mechanism is not limited to metal oxides and can be extended to other materials. In our samples, the low-bias resistance at low temperatures can well be accounted for by the Poole-Frankel model [18]:

$$R(T) = \frac{R(0)}{\left[(c * e^{[-(T_t/T)]})^n + 1\right]^{1/n}} \tag{1}$$

The fitting parameters $R(0)$, $T_t$, $c$, and $n$ are listed in Table I. For both films, the Poole-Frankel model describes the data remarkably well at temperatures below 100 K, as shown in Fig. 2(c).

The activation energy of the thin film is found to be 31 meV or $T_t = 360$ K. We do not observe considerable variation in the low-bias resistance in the thick film to reliably extract the activation energy. As we expect the nature of the traps to be similar in both films, we fixed the parameter $T_t$ at the same value. It is worth mentioning that the room-temperature low-bias electrical conductivity of the CNW films is of the order of $10^6$ S/m, which is much higher than that in typical NDR devices.
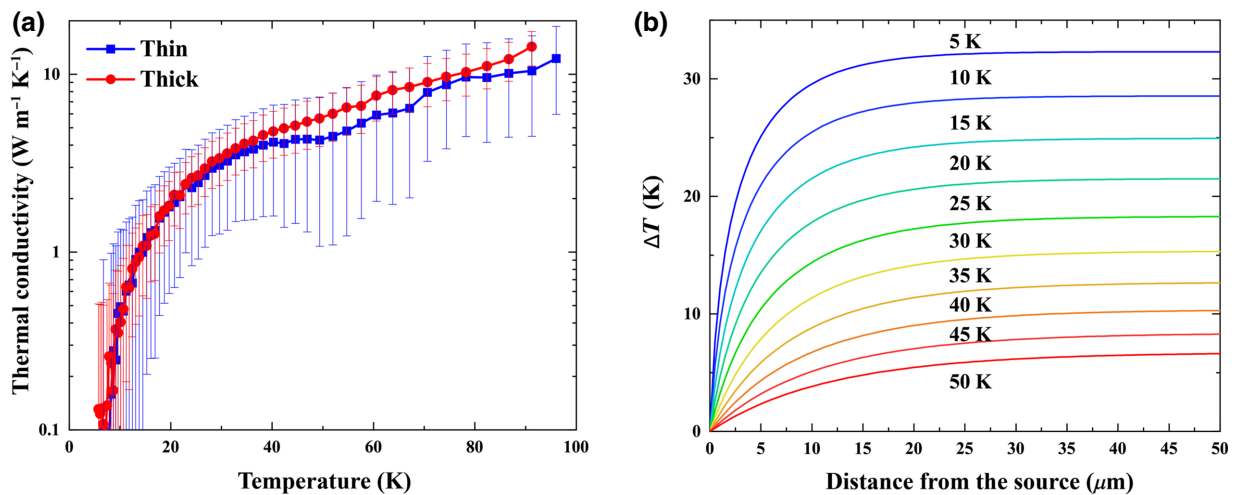


FIG. 3. (a) The measured thermal conductivity of CNWs film $\kappa_{CNW}$ by the steady-state longitudinal heat flow method and (b) simulated temperature variation along the channel near the metal contact. The temperature reaches its maximum on a length scale of a few tenths of micrometers.
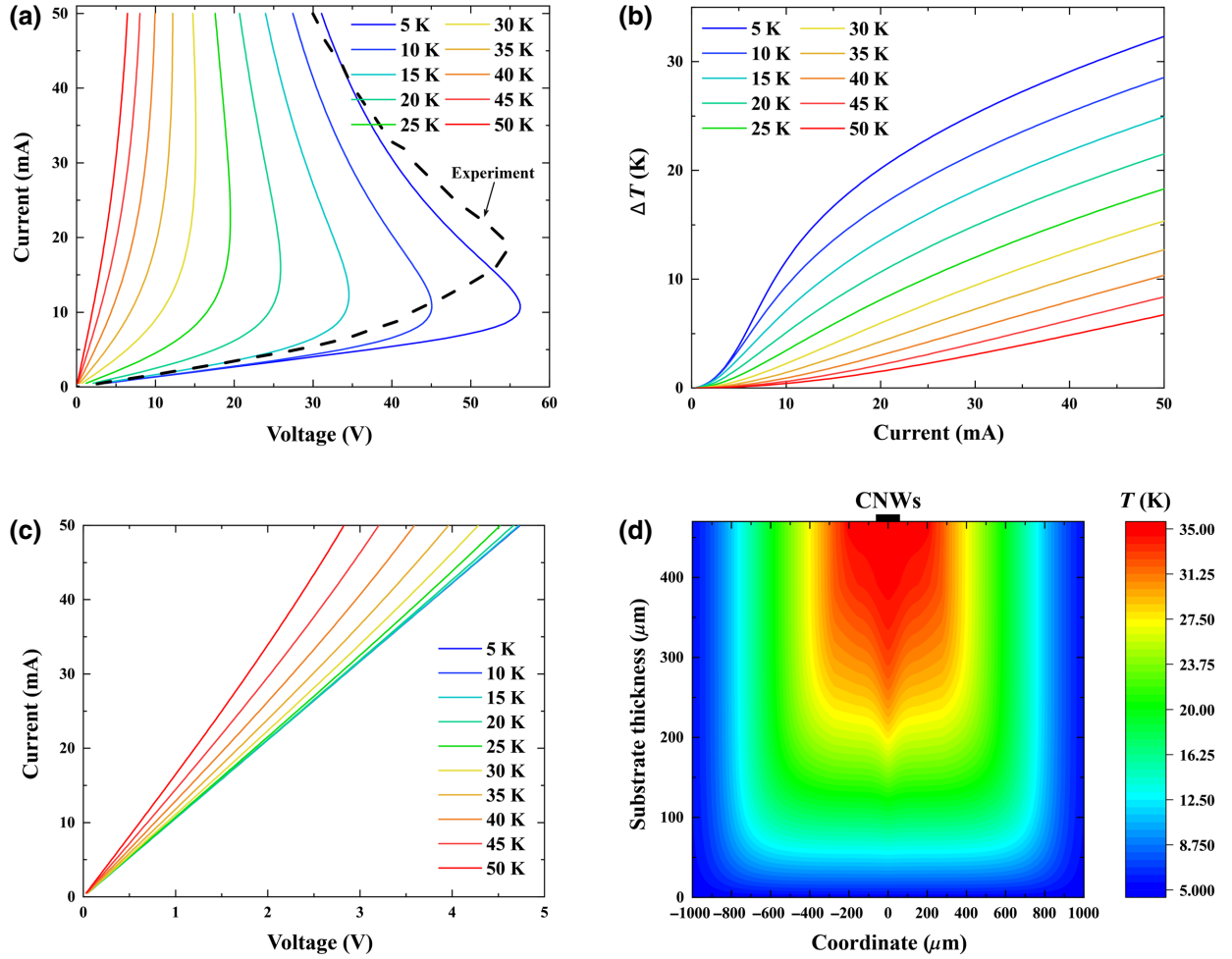
FIG. 4.  (a) Simulated *I-V* curves for the thin film at ambient temperatures from 5 to 50 K with a step of 5 K: from top to bottom, using $\kappa = 12\,000$ W/Km$^2$ as a single fitting parameter. The dashed curve shows experimental *I-V* with the most pronounced NDR. Although the overall agreement is rather good, some deviations are likely due to the temperature dependence of $\kappa$, which is not considered in our modeling. (b) The maximum temperature in the channel relative to the ambient temperature for the same conditions as in simulation in panel (a). (c) Simulated *I-V* curves for the thick film at ambient temperatures from 5 to 50 K with a step of 5 K: from top to bottom, using the same value of $\kappa$ and the experimental low-bias resistance *R(T)* from Fig. 2(c), (d) Two-dimensional simulation of the heat dissipation to the substrate, which is sitting of a stage at 5 K. The temperature of the CNWs film, shown by the black bar on top, is 35 K.

## IV. DISCUSSION

To simulate *I-V* characteristics at higher biases, we solve the self-consistently Fourier equation for the heat flow with the transport Ohm's law equation. The temperature variation along the channel of length $L = 40$ mm is given by

$$\frac{I^2 R[T(x)]}{\text{WL}} + \kappa_{\text{CNW}}[T(x)]h_{\text{CNW}} \frac{d^2 T(x)}{dx^2} - Q_{\text{sub}} = 0,$$

$$T(x = 0) = T(x = L) = T_0$$

(2)

where $T_0$ is the ambient temperature and $R(T)$ is the low-bias resistance from Fig. 2(c). The channel length is 40 mm

and the applied bias of 50 V would translate to the electric field of about 0.001 V/$\mu$m. Therefore, our devices are still in the low-bias regime operation. The first term in Eq. (2) gives the Joule losses. The current density is constant according to the continuity equation. The second term in Eq. (2) gives the in-plane heat dissipation across the film. We assume a constant temperature profile across the film.

The measured temperature dependence of the film's thermal conductivity $\kappa_{\text{CNW}}$ is shown in Fig. 3(a). The thermal conductivity of CNWs film $\kappa_{\text{CNW}}$ plays a critical role in establishing temperature distribution along the channel. The simulations of the temperature distribution along the channel are shown in Fig. 3(b). We find that temperature reaches its maximum value on a length scale of

TABLE II.   NDR characteristics of different material classes.

| | Materials | NDR type, mechanism | Current density (A/cm$^2$) | Peak-to-valley ratio | Temperature (K) | Ref. |
|---|---|---|---|---|---|---|
| Semiconductors | *Si based devices* | N, tunneling | $\sim$1000 | $\sim$2−4 | 300 | [54] |
| | *Ge based devices* | N, tunneling | $\sim$1000–16 000 | $\sim$7−10 | 300 | [54] |
| | *III-V based devices* | N, tunneling | $\sim$1300 | $\sim$20 | 300 | [54] |
| | *SiGe/Si* | N, tunneling | $\sim$0.2 | 7.6 | 300 | [55] |
| | GaN/AlN | N, tunneling | $\sim$7000 | 2.2 | 300 | [21] |
| | Si doped with Sb | S, Joule-heating | 0.1 | 1.3 | 1.9–2.5 | [56] |
| | *CaF$_2$/CdF$_2$* | N, tunneling | 63 | $\sim10^5$ | 300 | [57] |
| Organic molecules | Molecules | N, tunneling | $2.5 \times 10^5$ (25 nA per molecule)[a] | 15 | 6 | [7,24] |
| | Molecules | N, tunneling | $1.5 \times 10^4$ (1.5 nA per molecule)[a] | $\sim$10 | 300 | [7,23] |
| Oxides | VO$_2$ | N, electric-field-induced resistance switching | $\sim$40 000 | 2.3 | 300 | [14] |
| | VO$_2$ | S, Joule-heating-driven thermal phase transition | $\sim 1.7 \times 10^5$ | $\sim$1.5 | 300 | [58] |
| | TiO$_2$ | N, charge trapping/detrapping | $\sim$2000 | 1.7 | 300 | [17] |
| | TiO$_2$ | N, electrochemical reactions | $\sim$0.15 | $\sim$1.5 | 300 | [59] |
| | TaO$_x$ | S, Joule heating | $\sim$1000 | $\sim$3 | 300 | [18,59] |
| | Nb$_2$O$_5$/NbO$_x$ | S, Joule heating | $\sim$15 | 1.3 | 233–403 | [60] |
| | NbO$_x$ | S, Joule heating | $5 \times 10^6$ | 1.6 | 275–450 | [31] |
| | BaTiO$_3$ | N, charge trapping/detrapping | $\sim$2 | 1.5 | 300 | [15] |
| Layered materials | Black phosphorene/InSe | N, tunneling | $\sim$0.1 | 3 | 10–100 | [22] |
| | Graphene | N, electron-hole asymmetry in ambipolar regime | $\sim10^9$ ($\sim$2 mA/$\mu$m)[b] | 1.1 ($\sim$2.5) | 5 (300) | [9] |
| | Graphene nanoribbon | N, tunneling | $\sim10^7$ ($\sim$32 mA/mm)[b] | 5.9 | 300 | [61] |
| | graphene oxide | N, electrochemical reactions | $\sim10^5$ ($\sim$0.2 mA/mm)[b] | 2 | 300 | [39] |
| | Graphene/hBN/ Graphene | N, tunneling | 15 | 4 | 7/300 | [27] |
| | Graphene/WSe$_2$ | N, tunneling | 250/200 | 6/4 | 1.5/300 | [62] |
| | *Graphene/hBN/ Graphene* | N, tunneling | 26 | 2 | 2 | [63] |
| | *Graphene/hBN/ Graphene* | N, tunneling | 150 | 1.3 | 300 | [64] |
| | *Graphene/hBN/ Graphene* | N, tunneling | 0.03 | 1.3 | 300 | [65] |
| Carbon nanotubes | Single carbon nanotube | N, charge trapping/detrapping | $\sim10^5$ (10 nA per nanotube)[a] | 1.4 | 300 | [8] |
| | Suspended single carbon nanotube | N, Joule heating | $\sim10^8$ (10 $\mu$A per nanotube)[a] | $\sim$2 | 300 | [42] |
| Nanostructures | **CNWs** | **S, Joule heating** | **$10^5$** | **2** | **37** | **This work** |

[a]We assume the effective cross-section of a molecule and a carbon nanotube is 10 nm$^2$.
[b]We assume the effective thickness of graphene is 0.34 nm.

$L_c = 15 - 30 \ \mu$m from the metal contacts in our devices. These results demonstrate the potential of scaling of the channel lengths in these devices. Below $L_c$, NDR would be challenging to achieve due to the efficient heat sink of the metal electrodes.

The last term in Eq. (2) gives thermal dissipation to the substrate:

$$Q_{\mathrm{sub}} = \kappa[T(x) - T_0], \qquad (3)$$

where $\kappa$ is the effective thermal conductance, which includes both interfacial thermal conductance between the CNWs film and the substrate and the thermal conductance of the substrate itself. The latter can be estimated as $\kappa_{\mathrm{ox}}/t_{\mathrm{ox}}$, where $\kappa_{\mathrm{ox}}$ is the silicon substrate thermal conductivity of thickness $t_{\mathrm{ox}}$. The film cross-section can be found from the $W = 100 \ \mu$m and thickness $h_{\mathrm{CNW}} = 0.4$ or $1.0 \ \mu$m for the thin and thick films, correspondingly.

Once the temperature profile is calculated from Eqs. (2) and (3), Ohm's law gives the corresponding voltage drop across the channel: $V = (I/L) \int_0^L R[T(x)]dx$, as a function of current $I$.

The results of $I$-$V$ simulations for the thin CNWs film are shown in Fig. 4(a). Our simulations reproduce experimental results in Fig. 2(a) remarkably well and demonstrate that NDR behavior is caused by self-heating. The corresponding maximum temperatures in the channel as a function of current are shown in Fig. 4(b) for devices at different ambient temperatures. On the other hand, simulations in Fig. 4(c) with the experimental low-bias $R(T)$ from Fig. 2(c) for the thick CNW film do not demonstrate NDR behavior consistent with the experiment (not shown). The main reason for the linear $I$-$V$ characteristics in the latter case is the much weaker temperature dependence of the low-bias resistance.

Figure 4(d) shows the temperature distribution of the 100 $\mu$m channel at temperature 35 K sitting on the 470-$\mu$m-thick substrate. The latter is placed on a stage at a temperature of 5 K. The effective value of $\kappa$ is enhanced from a one-dimensional model result of $\kappa$ is enhanced from a one-dimensional model result $\kappa_{\mathrm{ox}}/t_{\mathrm{ox}}$ by a factor of $\alpha \approx 4.6$, where $\kappa_{\mathrm{ox}}$ is the silicon substrate thermal conductivity of thickness $t_{\mathrm{ox}}$. Therefore, our fitted value of $\kappa = 12\,000$ W/Km$^2$ would translate to $\kappa_{\mathrm{ox}} = \kappa t_{\mathrm{ox}}/\alpha \approx 1.2$ W/Km. This value of $\kappa_{\mathrm{ox}}$ is two orders of magnitude lower than the thermal conductivity of Si in the temperature range of interest here [66]. Therefore, interfacial thermal boundary resistance determines the thermal management of our devices. For two-dimensional graphene [67–69] lying flat on SiO$_2$ substrates, the interfacial thermal boundary conductance is reported in the range of MW/Km$^2$, which is also higher than our effective $\kappa$. The difference is due to our CNW material's morphology, shown in a revised Fig. 1(b), where an effective contact area is substantially reduced from a flat two-dimensional layer geometry.

In Table II, we compare the characteristics of our material with reported materials classes showing NDR behavior. The tunneling mechanism is primarily responsible for NDR in pioneering semiconducting materials. The switching time in tunneling devices is fast, and room-temperature operation is demonstrated. However, the on-currents are typically not that high. The molecular structures demonstrate NDR due to the tunneling mechanism with high current density per molecule. However, their integration is very challenging. A revived interest took place with the discovery of NDR with compelling characteristics in oxide materials. The dominant mechanisms, electrochemical reaction and Joule heating, are typically slower than the tunneling mechanism. Layered materials recently demonstrated NDR using various mechanisms, in which the low tunneling probabilities limit current densities and integration challenges of stacking layers need to be addressed.

The CNWs material reported here is easy to integrate and cheap to produce. The current densities are high, and the peak-to-valley ratio is reasonable. The microscopic mechanism for temperature dependence needs to be understood better to enable engineering activation energy in Eq. (1) to increase the operating temperature. The speed of operation is determined by the time needed to heat up and cool down the device. The switching time can be obtained from the time-dependent version of Eq. (2) with an additional term $h_{\mathrm{CNW}} C[dT(x, t)/dt]$ on the right-hand side of Eq. (2), where $C$ is electronic specific heat. Then Eq. (2) becomes a drift-diffusion equation with the effective diffusion coefficient $D = \kappa_{\mathrm{CNW}}[T(x)]/C$. Therefore, characteristic switching time can be estimated as $\tau \propto L^2/D = L^2 C/\kappa_{\mathrm{CNW}}$. Following Ref. [70], we can estimate electronic specific heat using the graphite value $C = 13.8 \ T \ \mu$J/(mol K) or 2.6 $T$ J/(m$^3$K) [71]. The time response of $\tau \propto 6$ ns can be estimated in a device with the channel length $L = L_c = 15 \ \mu$m (see Fig. 3b) and $\kappa_{\mathrm{CNW}} = 3$ W/mK at $T = 30$ K [see Fig. 3(a)]. This estimate implies that device operation is suitable near the microwave range (up to 0.2 GHz frequencies). Should the activation energy be engineered to enable room-temperature operation, the specific heat would increase proportionally by a factor of 10. At the same time, thermal conductivity, according to Fig. 3(a), would also increase by an order of magnitude, such that the time characteristics would be similar.

## V. CONCLUSIONS

Here we present a nanostructure class of materials demonstrating strong S-type NDR effects. CNWs maintain high current densities, unlike tunneling-based devices with NDR characteristics. The self-consistent electrical and thermal transport simulations prove that the heat sink to the substrate and the strong temperature dependence of

the low-bias resistance are the main reasons for the non-linear electrical behavior. Our studies suggest a pathway towards optimizing and controlling the NDR regime by the heat management and fabrication process of these electrical devices based on CNW low-dimensional materials. The simulations of the switching time suggest gigahertz frequency operation is possible in ultimately scaled devices. Further studies are needed to increase the operating temperature by engineering activation energy in CNWs.

## ACKNOWLEDGMENTS

[1] J. Chen, M. A. Reed, A. M. Rawlett, and J. M. Tour, Large on-off ratios and negative differential resistance in a molecular electronic device, Science **286,** 1550 (1999).

[2] L. Pellegrino, N. Manca, T. Kanki, H. Tanaka, M. Biasotti, E. Bellingeri, A. S. Siri, and D. Marré, Multistate memory devices based on free-standing $VO_2/TiO_2$ microstructures driven by joule self-heating, Adv. Mater. **24,** 2929 (2012).

[3] Y. Zhao, Z. Wan, X. Xu, S. R. Patil, U. Hetmaniuk, and M. P. Anantram, Negative differential resistance in boron nitride graphene heterostructures: Physical mechanisms and size scaling analysis, Sci. Rep. **5,** 10712 (2015).

[4] H. Mizuta and T. Tanoue, *The Physics and Applications of Resonant Tunnelling Diodes* (Cambridge University Press, Cambridge, 1995).

[5] L. Esaki, New phenomenon in narrow germanium P-n junctions, Phys. Rev. **109,** 603 (1958).

[6] J. B. Gunn, Microwave oscillations of current in III-V semiconductors, Solid State Commun. **1,** 88 (1963).

[7] N. J. Tao, Electron transport in molecular junctions, Nat. Nanotechnol. **1,** 173 (2006).

[8] M. Rinkiö, A. Johansson, V. Kotimaki, and P. Törmä, Negative differential resistance in carbon nanotube field-effect transistors with patterned gate oxide, ACS Nano **4,** 3356 (2010).

[9] Y. Wu, D. B. Farmer, W. Zhu, S.-J. Han, C. D. Dimitrakopoulos, A. A. Bol, P. Avouris, and Y.-M. Lin, Three-terminal graphene negative differential resistance devices, ACS Nano **6,** 2610 (2012).

[10] D. B. Strukov, G. S. Snider, D. R. Stewart, and R. S. Williams, The missing memristor found, Nature **453,** 80 (2008).

[11] Q. Xia and J. J. Yang, Memristive crossbar arrays for brain-inspired computing, Nat. Mater. **18,** 309 (2019).

[12] S. A. Chekol, J. Song, J. Park, J. Yoo, S. Lim, and H. Hwang, *Selector Devices for Emerging Memories* (LTD, Elsevier, Duxford, 2020), Ch. 5, p. 135.

[13] N. Balkan, B. K. Ridley, and A. J. Vickers, *Negative Differential Resistance and Instabilities in 2-D Semiconductors* (NATO ASI Series Colchester, UK, 1993).

[14] J. Sakai, High-efficiency voltage oscillation in $VO_2$ planer-type junctions with infinite negative differential resistance, J. Appl. Phys. **103,** 103708 (2008).

[15] G. Yang, C. H. Jia, Y. H. Chen, X. Chen, and W. F. Zhang, Negative differential resistance and resistance switching behaviors in $BaTiO_3$ thin films, J. Appl. Phys. **115,** 204515 (2014).

[16] B. G. Chae, H. T. Kim, D. H. Youn, and K. Y. Kang, Abrupt metal-insulator transition observed in $VO_2$ thin films induced by a switching voltage pulse, Phys. B Condens. Matter **369,** 76 (2005).

[17] Y. Du, H. Pan, S. Wang, T. Wu, Y. P. Feng, J. Pan, and A. T. S. Wee, Symmetrical negative differential resistance behavior of a resistive switching device, ACS Nano **6,** 2517 (2012).

[18] J. M. Goodwill, G. Ramer, D. Li, B. D. Hoskins, G. Pavlidis, J. J. McClelland, A. Centrone, J. A. Bain, and M. Skowronski, Spontaneous current constriction in threshold switching devices, Nat. Commun. **10,** 1628 (2019).

[19] S. Kumar and R. S. Williams, Separation of current density and electric field domains caused by nonlinear electronic instabilities, Nat. Commun. **9,** 2030 (2018).

[20] S. M. Bohaichuk, S. Kumar, G. Pitner, C. J. McClellan, J. Jeong, M. G. Samant, H. S. P. Wong, S. S. P. Parkin, R. S. Williams, and E. Pop, Fast spiking of a mott $VO_2$-carbon nanotube composite device, Nano Lett. **19,** 6751 (2019).

[21] Z. Vashaei, C. Bayram, and M. Razeghi, Demonstration of negative differential resistance in GaN/AlN resonant tunneling diodes at room temperature, J. Appl. Phys. **107,** 083505 (2010).

[22] Q. Lv, F. Yan, N. Mori, W. Zhu, C. Hu, Z. R. Kudrynskyi, Z. D. Kovalyuk, A. Patanè, and K. Wang, Interlayer band-to-band tunneling and negative differential resistance in van Der Waals BP/InSe field-effect transistors, Adv. Funct. Mater. **30,** 1910713 (2020).

[23] N. P. Guisinger, M. E. Greene, R. Basu, A. S. Baluch, and M. C. Hersam, Room temperature negative differential resistance through individual organic molecules on silicon surfaces, Nano Lett. **4,** 55 (2004).

[24] M. L. Perrin, R. Frisenda, M. Koole, J. S. Seldenthuis, J. A. C. Gil, H. Valkenier, J. C. Hummelen, N. Renaud, F. C. Grozema, J. M. Thijssen, D. Dulić, and H. S. J. Van Der Zant, Large negative differential conductance in single-molecule break junctions, Nat. Nanotechnol. **9,** 830 (2014).

[25] T. Li, X. Li, M. Tian, Q. Hu, X. Wang, S. Li, and Y. Wu, Negative transconductance and negative differential resistance in asymmetric narrow bandgap 2D-3D heterostructures, Nanoscale **11,** 4701 (2019).

[26] T. Roy, M. Tosun, X. Cao, H. Fang, D. H. Lien, P. Zhao, Y. Z. Chen, Y. L. Chueh, J. Guo, and A. Javey, Dual-gated $MoS_2/WSe_2$ van Der Waals tunnel diodes and transistors, ACS Nano **9,** 2071 (2015).

[27] L. Britnell, R. V. Gorbachev, A. K. Geim, L. A. Ponomarenko, A. Mishchenko, M. T. Greenaway, T. M. Fromhold, K. S. Novoselov, and L. Eaves, Resonant tunnelling and negative differential conductance in graphene transistors, Nat. Commun. **4,** 1794 (2013).

[28] V. K. Sangwan, D. Jariwala, I. S. Kim, K. S. Chen, T. J. Marks, L. J. Lauhon, and M. C. Hersam, Gate-tunable

memristive phenomena mediated by grain boundaries in single-layer $MoS_2$, Nat. Nanotechnol. **10,** 403 (2015).

[29] Y. An and Z. Yang, Abnormal electronic transport and negative differential resistance of graphene nanoribbons with defects, Appl. Phys. Lett. **99,** 192102 (2011).

[30] J. Huang, W. Wang, Q. Li, and J. Yang, Negative differential resistance devices by using N-doped graphene nanoribbons, J. Chem. Phys. **140,** 164703 (2014).

[31] G. A. Gibson, S. Musunuru, J. Zhang, K. Vandenberghe, J. Lee, C. C. Hsieh, W. Jackson, Y. Jeon, D. Henze, Z. Li, and R. Stanley Williams, An accurate locally active memristor model for S-type negative differential resistance in NbO$x$, Appl. Phys. Lett. **108,** 023505 (2016).

[32] A. S. Alexandrov, A. M. Bratkovsky, B. Bridle, S. E. Savel'Ev, D. B. Strukov, and R. Stanley Williams, Current-controlled negative differential resistance due to joule heating in $TiO_2$, Appl. Phys. Lett. **99,** 202104 (2011).

[33] Y. Yu, B. Zhao, J. M. Goodwill, Y. Ma, J. A. Bain, and M. Skowronski, Electrical and thermal dynamics of self-oscillations in $TaO_x$ -based threshold switching devices, ACS Appl. Electron. Mater. **2,** 683 (2020).

[34] B. K. Ridley, Specific negative resistance in solids, Proc. Phys. Soc. **82,** 954 (1963).

[35] G. A. Gibson, Designing negative differential resistance devices based on self-heating, Adv. Funct. Mater. **28,** 1704175 (2018).

[36] X. Zhong, X. Zhang, A. Gupta, and P. Leclair, Avalanche breakdown in microscale $VO_2$ structures, J. Appl. Phys. **110,** 084516 (2011).

[37] Z. Xiao, C. Ma, J. Huang, L. Liang, W. Lu, K. Hong, B. G. Sumpter, A. Li, and J. Bernholc, Design of atomically precise nanoscale negative differential resistance devices, Adv. Theory Simulations **2,** 1800172 (2019).

[38] K. M. M. Habib, F. Zahid, and R. K. Lake, Negative differential resistance in bilayer graphene nanoribbons, Appl. Phys. Lett. **98,** 192112 (2011).

[39] S. Rathi, I. Lee, M. Kang, D. Lim, Y. Lee, S. Yamacli, H. I. Joh, S. Kim, S. W. Kim, S. J. Yun, S. Choi, and G. H. Kim, Observation of negative differential resistance in mesoscopic graphene oxide devices, Sci. Rep. **8,** 7144 (2018).

[40] S. L. Rumyantsev, G. Liu, M. S. Shur, and A. A. Balandin, Observation of the memory steps in graphene at elevated temperatures, Appl. Phys. Lett. **98,** 222107 (2011).

[41] E. Pop, D. Mann, Q. Wang, K. Goodson, and H. Dai, Thermal conductance of an individual single-wall carbon nanotube above room temperature, Nano Lett. **6,** 96 (2006).

[42] E. Pop, D. Mann, J. Cao, Q. Wang, K. Goodson, and H. Dai, Negative Differential Conductance and Hot Phonons in Suspended Nanotube Molecular Wires, Phys. Rev. Lett. **95,** 155505 (2005).

[43] V. Nam Do and P. Dollfus, Negative differential resistance in zigzag-edge graphene nanoribbon junctions, J. Appl. Phys. **107,** 063705 (2010).

[44] H.-S. Choo, T. Kinumoto, Y. Iriyama, T. Abe, and Z. Ogumi, Mechanism for electrochemical oxidation of highly oriented pyrolytic graphite during potential cycling in sulfuric acid solution, ECS Trans. **11,** 1003 (2019).

[45] S. A. Evlashin, F. S. Fedorov, P. V. Dyakonov, Y. M. Maksimov, A. A. Pilevsky, K. I. Maslakov, Y. O. Kuzminova,

Y. A. Mankelevich, E. N. Voronina, S. A. Dagesyan, V. A. Pletneva, A. A. Pavlov, M. A. Tarkhov, I. V. Trofimov, V. L. Zhdanov, N. V. Suetin, and I. S. Akhatov, Role of nitrogen and oxygen in capacitance formation of carbon nanowalls, J. Phys. Chem. Lett. **11,** 4859 (2020).

[46] P. Dyakonov, K. Mironovich, S. Svyakhovskiy, O. Voloshina, S. Dagesyan, A. Panchishin, N. Suetin, V. Bagratashvili, P. Timashev, E. Shirshin, and S. Evlashin, Carbon nanowalls as a platform for biological SERS studies, Sci. Rep. **7,** 13352 (2017).

[47] S. Evlashin, S. Svyakhovskiy, N. Suetin, A. Pilevsky, T. Murzina, N. Novikova, A. Stepanov, A. Egorov, and A. Rakhimov, Optical and IR absorption of multilayer carbon nanowalls, Carbon N. Y. **70,** 111 (2014).

[48] V. A. Krivchenko, S. A. Evlashin, K. V. Mironovich, N. I. Verbitskiy, A. Nefedov, C. Wöll, A. Y. Kozmenkova, N. V. Suetin, S. E. Svyakhovskiy, D. V. Vyalikh, A. T. Rakhimov, A. V. Egorov, and L. V. Yashina, Carbon nanowalls: The next step for physical manifestation of the black body coating, Sci. Rep. **3,** 3328 (2013).

[49] N. V. Minaev, M. A. Tarkhov, D. S. Dudova, P. S. Timashev, B. N. Chichkov, and V. N. Bagratashvili, Fabrication of superconducting nanowire single-photon detectors by nonlinear femtosecond optical lithography, Laser Phys. Lett. **15,** 026002 (2018).

[50] A. V. Inyushkin, A. N. Taldenkov, V. G. Ralchenko, A. P. Bolshakov, A. V. Koliadin, and A. N. Katrusha, Thermal conductivity of high purity synthetic single crystal diamonds, Phys. Rev. B **97,** 144305 (2018).

[51] L. G. Caņado, K. Takai, T. Enoki, M. Endo, Y. A. Kim, H. Mizusaki, A. Jorio, L. N. Coelho, R. Magalhães-Paniago, and M. A. Pimenta, General equation for the determination of the crystallite size La of nanographite by Raman spectroscopy, Appl. Phys. Lett. **88,** 1998 (2006).

[52] A. C. Ferrari and D. M. Basko, Raman spectroscopy as a versatile tool for studying the properties of graphene, Nat. Nanotechnol. **8,** 235 (2013).

[53] Y. Wu, B. Yang, B. Zong, H. Sun, Z. Shen, and Y. Feng, Carbon nanowalls and related materials, J. Mater. Chem. **14,** 469 (2004).

[54] P. R. Berger and A. Ramesh, Negative differential resistance devices and circuits, Compr. Semicond. Sci. Technol. **1–6,** 176 (2011).

[55] Y. Suda and H. Koyama, Electron resonant tunneling with a high peak-to-valley ratio at room temperature in $Si_{1−x}Ge_x$/Si triple barrier diodes, Appl. Phys. Lett. **79,** 2273 (2001).

[56] A. L. Danilyuk, A. G. Trafimenko, A. K. Fedotov, I. A. Svito, and S. L. Prischepa, Negative differential resistance in N-type noncompensated silicon at Low temperature, Appl. Phys. Lett. **109,** 222104 (2016).

[57] M. Watanabe, Y. Iketani, M. Asada, I. B. Epitaxy, M. Watanabe, Y. Aoki, R. T. Diodes, M. Maeda, and S. Watanabe, Related content $CaF_2/CdF_2$ double-barrier resonant tunneling diode with high room-temperature peak-to- valley ratio, Jpn. J. Appl. Phys. **39,** L716 (2000).

[58] S. Kumar, M. D. Pickett, J. P. Strachan, G. Gibson, Y. Nishi, and R. S. Williams, Local temperature redistribution and structural transition during joule-heating-driven conductance switching in $VO_2$, Adv. Mater. **25,** 6128 (2013).

[59] Y. Kim, J. H. Jang, S. J. Park, S. Jesse, L. Donovan, A. Y. Borisevich, W. Lee, and S. V. Kalinin, Local probing of electrochemically induced negative differential resistance in TiO$_2$ memristive materials, Nanotechnology **24,** 085702 (2013).

[60] S. Slesazeck, H. Mähne, H. Wylezich, A. Wachowiak, J. Radhakrishnan, A. Ascoli, R. Tetzlaff, and T. Mikolajick, Physical model of threshold switching in NbO$_2$ based memristors, RSC Adv. **5,** 102318 (2015).

[61] P. D. Nguyen, T. C. Nguyen, F. M. Hossain, D. H. Huynh, R. Evans, and E. Skafidas, Negative differential resistance effect in planar graphene nanoribbon break junctions, Nanoscale **7,** 289 (2015).

[62] G. W. Burg, N. Prasad, B. Fallahazad, A. Valsaraj, K. Kim, T. Taniguchi, K. Watanabe, Q. Wang, M. J. Kim, L. F. Register, and E. Tutuc, Coherent interlayer tunneling and negative differential resistance with high current density in double bilayer graphene-WSe$_2$ heterostructures, Nano Lett. **17,** 3919 (2017).

[63] A. Mishchenko, et al., Twist-controlled resonant tunnelling in graphene/boron nitride/graphene heterostructures, Nat. Nanotechnol. **9,** 808 (2014).

[64] K. Kim, M. Yankowitz, B. Fallahazad, S. Kang, H. C. P. Movva, S. Huang, S. Larentis, C. M. Corbet, T. Taniguchi, K. Watanabe, S. K. Banerjee, B. J. Leroy, and E. Tutuc, Van Der Waals heterostructures with high accuracy rotational alignment, Nano Lett. **16,** 1989 (2016).

[65] B. Fallahazad, K. Lee, S. Kang, J. Xue, S. Larentis, C. Corbet, K. Kim, H. C. P. Movva, T. Taniguchi, K. Watanabe, L. F. Register, S. K. Banerjee, and E. Tutuc, Gate-tunable resonant tunneling in double bilayer graphene heterostructures, Nano Lett. **15,** 428 (2015).

[66] M. Asheghi, K. Kurabayashi, R. Kasnavi, and K. E. Goodson, Thermal conduction in doped single-crystal silicon films, J. Appl. Phys. **91,** 5079 (2002).

[67] M. Freitag, M. Steiner, Y. Martin, V. Perebeinos, Z. Chen, J. C. Tsang, and P. Avouris, Energy dissipation in graphene field-effect transistors, Nano Lett. **9,** 1883 (2009).

[68] K. F. Mak, C. H. Lui, and T. F. Heinz, Measurement of the thermal conductance of the graphene/ SiO$_2$ interface, Appl. Phys. Lett. **97,** 221904 (2010).

[69] Y. K. Koh, M. H. Bae, D. G. Cahill, and E. Pop, Heat conduction across monolayer and few-layer graphenes, Nano Lett. **10,** 4363 (2010).

[70] N. R. Pradhan, H. Duan, J. Liang, and G. S. Iannacchione, The specific heat and effective thermal conductivity of composites containing single-wall and multi-wall carbon nanotubes, Nanotechnology **20,** 245705 (2009).

[71] T. Nihira and T. Iwata, Temperature dependence of lattice vibrations and analysis of the specific heat of graphite, Phys. Rev. B - Condens. Matter Mater. Phys. **68,** 134305 (2003).

[72] http://hdl.handle.net/10477/79221.